Multi Modal Fingertip Elastography and Reconstruction Methods

by

Altaf A. Khan
B.S. (University of Illinois at Chicago) 2010

Thesis submitted in partial fulfillment of the requirements
for the degree of Doctor of Philosophy in Mechanical Engineering
in the Graduate College of the
University of Illinois at Chicago, 2018

Chicago, Illinois

Defense Committee:
Thomas J. Royston, Chair and Advisor, Bioengineering and Mechanical Engineering
Dieter Klatt, Bioengineering
Richard Magin, Bioengineering
Michael Scott, Mechanical Engineering
Craig Foster, Civil Engineering

To my family

ACKNOWLEDGMENTS

It would be impossible for me to spend 8 years in the graduate program without the help and support of many people. Without them, I could never have completed my work.

First, I want to thank those directly involved in my research starting with my advisor Dr. Royston, who has guided me through every stage of my academic career. He has shown me that being a successful engineer is not only about the work you do but how you make time for family and those in need. Thank you to Drs. Dieter Klatt and Richard Magin, in helping me through understanding biomechanics. As a mechanical engineer, working in a field that is different than your degree can be challenging but they have given me the tools I needed to succeed. Thank you to Dr. Craig Foster for his advanced courses on finite element analysis without which I would still be solving an analytical equation. Thank you to Theodore Claiborne who was essential in developing a working RF coil, an art that so few are capable of creating. Thank you to Weiguo Li and Jin Gao for putting up with my constant unscheduled "5 minute" experiments at the MRI facility that took over an hour. Thank you to Eric Schmidt and David Mecha at the UIC Engineering machine shop who have taught me how to design something that can be manufactured as well as building countless fixtures needed for my projects. And thank you to my labmates, Kaya Yasar, Steve Kearney, Spencer Brinker, Yifei Liu, Allen Ye, Ziying Yin who were integral to developing the skills I need to create the experiments and skills presented in this dissertation.

ACKNOWLEDGMENTS (Continued)

I would also like to thank those at UIC who have complemented my experiences not relevant to research such as teaching and student affairs. Thank you to Dr. Michael Scott for allowing me to take on elevated teaching positions to gain experiences needed as a professor as well as Dr. Jamie Szwalek for mentoring me through the process of teaching. Thank you to the several RDs I worked with in Campus Housing as well as Dr. Nick Ardinger and Priscilla Velarde for supporting me through the more difficult times of my research.

Lastly I would like to thank those who still don't quite know what it is I exactly do. Thanks to my friends who have supported me when I was struggling even if that meant not to ask me about my research. Thank you to Tom Seymour and Suzie Helmerci for helping me relax through the joys of comics. Thank you to the karate instructors who have provided me with an outlet for my stress in a healthy fashion. And finally, thank you to my family who have given me every opportunity that allowed me to pursue this degree. I sincerely could not have done anything without their support.

And I guess thank you to you for reading this.

CONTRIBUTION OF AUTHORS

Chapter 1 is a review of literature pertaining to the topic covered in my dissertation as well as presenting the motivation for why my research is relevant. Chapters 2 and 3 represent a published article (1). Dr. Steven P. Kearney designed the analytical approximation code in Matlab covered in Chapter 2 and, along with my advisor Dr. Thomas J. Royston, assisted in the writing of the article. Chapters 4 and 5 contain a series of unpublished experiments completed by myself that lay out the groundwork for future projects to be continued in the lab after my graduation. Chapter 6 is the final conclusions drawn from my research and the prospects of future work.

TABLE OF CONTENTS

TABLE OF CONTENTS (Continued)

CHAPTER **PAGE**

LIST OF TABLES

LIST OF FIGURES

LIST OF ABBREVIATIONS

FE	Finite Element
FEA	Finite Element Analysis
FOV	Field of View
GF	Geometrically Focused
MEG	Motion Encoding Gradient
MRE	Magnetic Resonance Elastography
MRI	Magnetic Resonance Imaging
OCT	Optical Coherence Tomography
RF	Radio Frequency
SLDV	Scanning Laser Doppler Vibrometry
SLIM	SampLe Interval Modulation MRE
SNR	Signal to Noise Ratio

SUMMARY

This dissertation details the research of elastography applied specifically to the human fingertip. Vibrations are induced on the surface of the fingertip and resulting wave propagation is measured to recreate mechanical properties such as shear modulus. In particular, three methods were used to measure wave propagation, Scanning Laser Doppler Vibrometry (SLDV), Magnetic Resonance Imaging (MRI), and Optical Coherence Tomography (OCT). All methods used Geometric Focused (GF) waves. GF waves use a annular ring actuator on the surface to produce converging waves to a focus point. Previous lab work used analytical equations to approximate the shear modulus. However, throughout the project, it was determined that the analytical solution proved to be invalid and a new post processing method to determine shear modulus was developed using Finite Element Analysis (FEA).

For SLDV measurements, an actuator was designed to apply vibrations to the surface of the fingertip while maintaining line of sight for the equipment to measure wave propagation through a laser. Measured wave propagations were originally post processed using MATLAB code to estimate shear modulus. However, the governing equations used proved invalid for surface waves. Thus the development of FE-based optimization.

FE-based optimization involved the creation of a 3D model of the human fingertip. The model was assigned initial material properties, boundary conditions, and displacement equal to the actuation used in previous method. The resulting wave propagation is compared to the experimental results through an error function. Then the material properties are varied

to optimize the match of simulated to experimental wave propagation. Although results were better, more research needed to be done on the underlying tissue in the fingertip to accurately estimate shear modulus.

OCT was used to measure waves directly below the surface of the fingertip. Using the same actuator design as the SLDV setup, vibrations were applied to the surface of the fingertip at 100 Hz. OCT took images of the finger at 93 Hz. The slight difference in frequency allows the measuring of waves using the strobe effect. Although a much smaller region of the finger can be measured, being able to measure wave propagation directly below the surface gave insight into the interaction between surface skin and its underlying layers.

For MRI measurements, a completely new actuator design needed to be created. Due to the constraints of working in an MRI, primarily no magnetic components, small bore size, and standard Radio Frequency (RF) coils shape, it was difficult to apply actuation directly and normal to the surface to the fingertip. Therefore, a new surface coil was built that incorporated the actuator in its design. The coil allows the actuator to be placed directly on the surface that is being imaged and produces stronger waves. Results show that the underlying fat tissue of the fingertip creates more complex wave patterns due to diffraction and reflections.

CHAPTER 1

INTRODUCTION

1.1 Medical Motivation

Viscoelastic properties of human skin are affected by disease and injury; measurement of these properties may be used as a diagnostic aid for detection and monitoring of conditions that affect the epidermis and dermis. For example, Raynaud's phenomena and scleroderma have been shown to increase shear elasticity and shear viscosity (2; 3), as well as affect the thickness of skin (4). However, skin viscoelastic properties are also affected by ambient temperature, humidity, moisture content (5; 6), thickness, age (7; 8; 9), sex, and the direction of applied stress (10). These confounders have limited the utility of elastography measurements.

Early measurement methods relied mainly on excised strips of skin and tensometer equipment (7). These tests were accurate and could be performed alongside histological analysis to correlate the stress-strain relationship with changes in molecular structure. However, this was too invasive to be used as a diagnostic tool for skin disorders. Advances in more sensitive measuring equipment led to in vivo measurements of shear strain hysteresis curves (5). Up to this point, the majority of the studies were based on static methods until (6) studied the dynamic viscoelastic properties of skin, over a frequency range of near zero to 1000 Hz, using propagating surface waves. It was found that the viscoelastic properties were dispersive (frequency-dependent). A similar study also found comparable results; using surface wave

propagation, a direct measurement of the complex Young's modulus of excised rabbit skin was calculated (11). Even though it has been determined that skin is viscoelastic, static methods, such as the suction method or indentation method, have proven reliable and practical for clinical use (10; 12; 13; 14); however, they cannot measure the frequency dependence or viscous behavior, which is potentially an additional biomarker.

Focusing on the dynamic response of skin, elastography techniques have been developed that use surface waves as the source for elastography imaging. Elastography uses the principle that the wavelength and attenuation of a propagating mechanical wave is dependent on the mechanical properties. Using this principle, several imaging modalities have been used to estimate shear viscoelastic properties. Optical coherence elastography (OCE) has been used to measure skin viscoelasticity (15; 16), and excised animal tissue (17). OCE has the advantages of micrometer scale resolution, and 3D imaging capabilities, with limited surface penetration. Optical elastography (OE) based on laser Doppler vibrometry has the advantage of high SNR due to the sensitivity of LASER probes, but it cannot penetrate the surface. Also, most OE methods for skin measure waves that are propagating radially away from a vibratory point source which suffer significantly from attenuation, due to geometric dispersion thus limiting the bandwidth of measurement.

In a recent article by Kearney *et al.* (18) optical measurement of geometrically focused (GF) waves was introduced that allows for wider bandwidth measurements. An analytical solution for the case of a radiating annular disk surface source was fit to experimentally measured GF surface waves, enabling an estimate of the frequency-dependent complex-valued surface wavenumber,

which can then be related to the dynamic complex-valued shear modulus. Several viscoelastic models were then fit to the dynamic shear modulus dispersion curve measured on the forearm of healthy volunteers. Viscoelastic models were evaluated based on their overall quality of fit and variability.

In this dissertation, the analytical solution has been identified as an inaccurate model for GF surface waves. A number of previous dynamic elastography studies have used numerical optimization approaches, some involving finite element approximations of the experimental system, to identify multiple and/or complex shear viscoelastic parameters simultaneously (19; 20). In this dissertation, a new approach is proposed using a finite element (FE) model of the finger. Material properties of the model are optimized by curve fitting the FE results to the experimental wave profiles measured using scanning laser doppler vibrometer (SLDV). Further improvements to the method were studied such as the introduction of skin layers to the FE model.

A recent study by Zhang (21) has also introduced a dynamic elastography approach to quantify the stiffness of the skin on the fingertip using an optical approach, a type of laser displacement sensor. The phase gradient cross spectrum method is used to estimate the propagation speed of Rayleigh (surface) waves generated via a 100 Hz harmonic excitation. While using a related, but different means of generation and acquisition of surface wave motion on the fingertip, some of the same issues addressed in this dissertation, with respect to identification of shear storage and loss moduli, choice of rheological model and other modeling assumptions, are relevant regardless of differences in means of surface wave generation and measurement.

1.2 Sensory Tactile Motivation

Physical touch is one of the most basic ways humans interact with the world. Fingertips heavily impact the touch perception. Understanding the mechanical properties of the fingertip is essential to manipulating touch perception. For example, a rough surface can be made to feel smooth or rough because of vibrations at a certain frequency. The early work of Watanabe and Fukui showed that a surface that undergoes a normal displacement at low ultrasonic frequency sees its friction decreased when explored with a bare fingertip (22). But, the skin and subcutaneous tissues of the fingertip are far from rigid. As a consequence, the surface wave created by a harmonic excitation of 20 to 40 kHz has a wavelength on the order of one millimeter. The wavelength is approximately one order of magnitude lower than the diameter of a typical contact patch between the fingertip and a flat surface (22). Further studies have shown that increase in amplitude of vibrations reduces the true contact area between the fingertip and the surface as well as the interfacial friction (23). Consequently, there is an interest in determining the viscoelastic properties of the skin on the fingertip in the range of frequencies spanning from tactile exploration (100 Hz) through the lower end of the ultrasonic frequencies ($<$ 100 kHz).

1.3 Intellectual Merit

The research applies and advances techniques of elastography and reconstruction methods, applying them to the finger, a challenging target given its small size, rounded shape, heterogeneity and anisotropy. Different methods of measurements, SLDV, OCT, and MRI, allow for seeing mechanical wave propagation at different depths of the finger. Additionally, a wide range of frequencies can be used in each method to identify the optimal viscoelastic model of

the fingertip. The use of FE-based optimization allows for a more accurate modeling due to its geometric design and controlled boundary conditions. Multiple studies allow for study of variability between healthy humans and repeatability to see the effects of room temperature and humidity on the material properties.

1.4 Broader Impact of Study

The main goal of this study is the quantitative analysis of the material properties of the human finger. Noninvasive methods to estimate the mechanical properties of the finger allows us to study the effects of vibrations on the finger for use in haptic feedback. The methodological advances in elastography that are developed could be adapted and applied to different areas of interest, including other locations on the skin surface to quantify diseases, such as scleroderma, in order to develop early diagnosis methods. Using multiple modes of measurements, SLDV, OCT, and MRI, allows for a unique opportunity to measure wave propagation at different depths: surface, near surface, and subdermal. Being able to correlate the three can lead to a better mechanical model of tissues and organs. MRE has been used to measure wave propagation in different tissues in the body. However, limitations of MRI prevent the most direct application of vibration on the surface causing loss of wave motion. Creating RF coils that incorporate the equipment necessary for MRE can improve elastography sensitivity. Reconstruction methods in elastography have proven to be a challenge. General approximations are made based on assumptions of infinite or semi-infinite homogenous mediums. Developing an FE-based optimization method for reconstruction allows for complex analysis of the finger and can further be applied to other tissues and organs composed of multiple materials and unique

shapes. Understanding the mechanical properties of any organ can be used to diagnose healthy ranges as well as fabricating synthetic materials with similar properties.

1.5 Aims

This dissertation will cover three aims. Each chapter will briefly explain any relevant theory, the methods and working principles of the experiment, and results and discussion. A broad conclusion of the aims will be made at the end of the dissertation.

Aim 1: develop a novel actuator design to apply vibrations to the fingertip surface to measure wave propagation at multiple frequencies using Scanning Laser Doppler Vibrometry and approximate shear modulus of the fingertip.

Aim 2: development of FE-based optimization to reconstruct material properties based on measurements from SLDV experiments.

Aim 3: further implementation of actuator design and application for use with Optical Coherence Tomography to measure wave propagation in the underlying skin layers.

Aim 4: develop a novel Radio Frequency coil with an incorporated actuator to induce and measure wave propagation throughout the fingertip.

CHAPTER 2

SCANNING LASER DOPPLER VIBROMETRY ON FINGERTIP SURFACE

(Previously published as Khan, A., Kearney, S., Royston, T. (2018) Finite Element Based Optimization of Human Fingertip Optical Elastography, J. Medical Diagnostics 1(3), 031007)

2.1 Background

SLDV uses the Doppler Effect on lasers to measure the velocity of a surface. Adding several measuring points on the surface allows the scanning of the surface wave propagation. SLDV is useful for measuring wave propagation on the surface of most materials as well as being able to measure the source of the actuation. The results are given as a complex-valued displacement showing oscillation over time. The complex-valued displacement is used to reconstruct material properties such as shear stiffness. When working with SLDV, it is important that the laser has a clear line of sight on the area being measured.

2.2 Theory: Analytical approximation for geometrically focused surface waves

The steady state exact analytical solution for geometrically focused (GF) shear waves that are radially converging over a linear isotropic viscoelastic cylindrical volume can be found in Yasar et al. (24) and is:

$$u_z(r,t,k_s) = u_z(a)\frac{J_0(rk_s)}{J_0(ak_s)}e^{j\omega t} \tag{2.1}$$

where J_0 is the Bessel function of the first kind and zeroth order, r is the radial distance from the central axis, k_s is the complex-valued shear wavenumber, a is the radius of the cylinder, ω is frequency in radians/sec, u_z is the displacement amplitude in the axial (z) direction, and $u_z(a)$ is the magnitude of the displacement amplitude in the axial (z) direction at $r = a$.

This can also be expressed as a frequency response function (FRF) relating vertical (axial) motion $u_z(r)$ at a radial location $r < a$ to the imposed vertical motion $u_z(a)$ at the outer boundary of the cylinder $r = a$ as follows:

$$FRF = \frac{u_z(r)}{u_z(a)} = \frac{J_0(rk_s)}{J_0(ak_s)} \tag{2.2}$$

Previously, in Kearney et al. (18), by analogy to Yasar et al. (24) and in comparison to the theory for outward traveling surface waves driven by a disk of radius a derived in Royston et al. (25), the following FRF was proposed to relate steady state vertical (normal) motion $u_z(r)$ at a radial location $r < a$ to the imposed vertical motion $u_z(a)$ at $r = a$ on a surface driven normally by an annular (ring-shaped) actuator of inner radius r=a.

$$FRF = \frac{u_z(r)}{u_z(a)} = \frac{I_0(jrk_{su})}{I_0(jak_{su})}, \tag{2.3}$$

Here, I_0 is the modified Bessel function of the first kind and zeroth order, k_{su} denotes the complex-valued Rayleigh (surface) wave number, whose real part correlates with surface wave phase speed and whose imaginary part is linked to surface wave attenuation due to viscous losses.

Soft biological tissue can be considered as nearly incompressible since the bulk modulus is similar to that of water and is as much as six orders of magnitude larger than the tissue's shear and Young's moduli. This results in a Poisson's ratio ν approaching, but not reaching, 0.5. Using ν=0.49995 we have the following approximation from Graff (26) relating shear and surface wavenumbers:

$$\frac{k_{su}}{k_s} = \frac{0.87 + 1.12\nu}{1 + \nu} \approx 0.95 \tag{2.4}$$

This suggests then that if one can estimate the complex surface wavenumber by fitting Equation 3.1 to measured steady state GF surface wave motion, then by Equation 2.4 one can estimate the complex shear wave number. This is in turn can be used to estimate the complex shear modulus $\mu = \mu_R + j\mu_I$, where μ_R and μ_I denote shear storage and loss moduli, respectively, as

$$k_s = \omega\sqrt{\frac{\rho}{\mu}}. \tag{2.5}$$

where ρ is the tissue density.

2.3 Viscoelastic Models

Once the complex shear modulus at multiple frequencies has been estimated, different linear viscoelastic models can be fit to it. The value of identifying an appropriate rheological (viscoelastic) model by fitting the complex shear moduli obtained at multiple frequencies is that it enables one to predict moduli at other frequencies not measured in the experiment. Addi-

tionally, it potentially provides insight into the structure of the material. Candidate rheological models considered in this study are introduced in Figure 1.

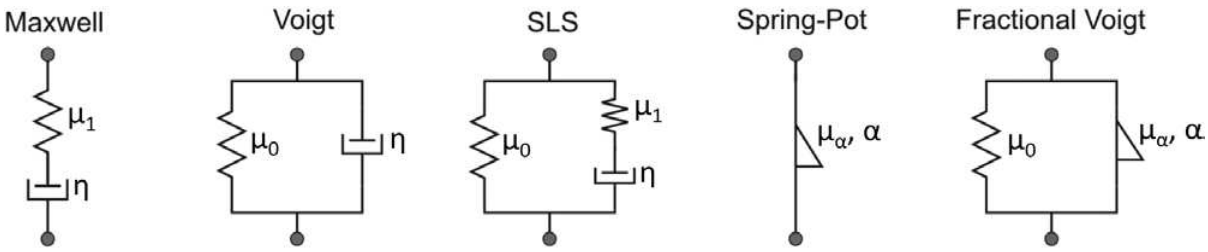

Figure 1: Shear viscoelastic models used for study

The shear storage modulus, μ_R, and loss modulus, μ_I for these viscoelastic models can be seen in Table I.

TABLE I: Shear storage and loss moduli for selected viscoelastic models

Viscoelastic Model	Storage Modulus μ_R	Loss Modulus μ_I
Maxwell	$\frac{\omega^2\eta^2\mu_1}{\mu_1^2+\omega^2\eta^2}$	$\frac{\omega\eta\mu_1^2}{\mu_1^2+\omega^2\eta^2}$
Voigt	μ_0	$\omega\eta$
SLS	$\frac{\mu_0\mu_1^2+\omega^2\eta^2(\mu_0+\mu_1)}{\mu_1^2+\omega^2\eta^2}$	$\frac{\omega\eta\mu_1^2}{\mu_1^2+\omega^2\eta^2}$
Spring-pot	$\mu_\alpha\omega^\alpha\cos(\frac{\pi}{2}\alpha)$	$\mu_\alpha\omega^\alpha\sin(\frac{\pi}{2}\alpha)$
Fractional Voigt	$\mu_0+\mu_\alpha\omega^\alpha\cos(\frac{\pi}{2}\alpha)$	$\mu_\alpha\omega^\alpha\sin(\frac{\pi}{2}\alpha)$

2.4 Methods

2.4.1 Experimental Setup

The annular actuator imparts a ring of dynamic displacement around the fingertip that generates radially converging surface waves. As the waves converge toward the center, they add constructively to counteract attenuation due to viscosity. This allows motion to be measured over a broader frequency range.

A three-dimensional model of an actuator was created using Autodesk Inventor Professional. The model was printed using titanium alloy via Materialise (Leuven, Belgium) and is shown in Figure 2. It contains a 10 mm ring for actuating and a hole for line of sight necessary for Scanning Laser Doppler Vibrometer (SLDV) measurements. The actuator is connected to a piezo-ceramic stack from Physik Instrumente GmbH & Co. (Karlsruhe, Germany) 7 x 7 x 36 mm which provides 30 μm displacement at 100 volts. The other end of the piezo-ceramic stack is connected to the ground via a tabletop breadboard. The study volunteer inserts their finger into the actuator and gently presses up against the ring. Their wrist rests on an elevated surface to keep the arm level and comfortable.

A sinusoidal 3 Volts peak-to-peak (V_{PP}) waveform is created using an internal function generator on the SLDV computer. The waveform is sent to an amplifier (Yamaha Power Amplifier P3500S, Buena Park, CA, USA) to bring amplitude to 40 V_{PP}. This is applied to the piezo ceramic stack along with a 20 volt DC bias (BK Precision 1672, Yorba Linda, CA, USA) to prevent damage to the actuator caused by applying a negative charge.

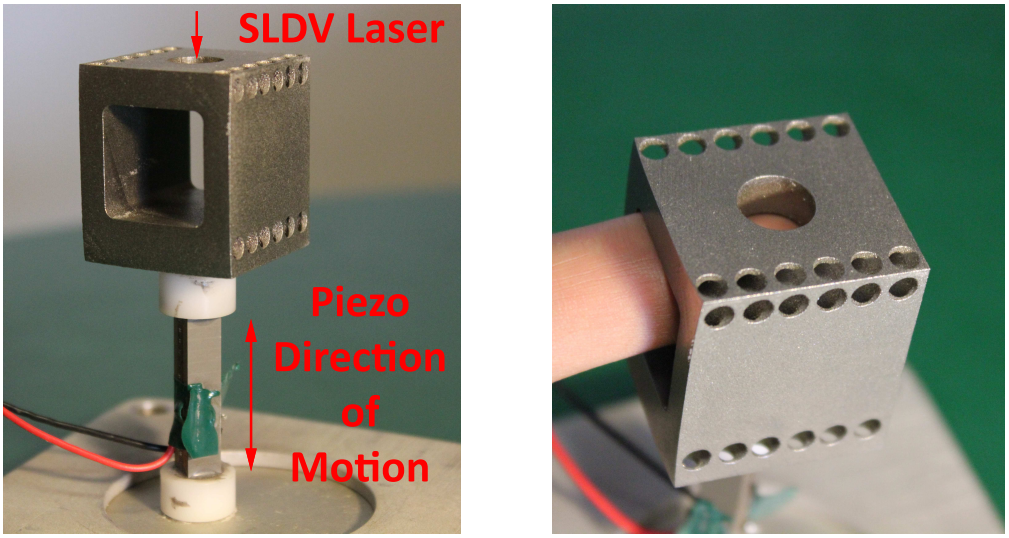

Figure 2: Titanium alloy actuator (left) with arrows showing direction of motion and line of sight required by SLDV (right) showing finger in actuator

The SLDV (Polytec PSV-400, Irving, CA, USA) is set up to measure a single line across the surface of the fingertip along an internal radius of the actuator. About 60 equispaced points are used along the radius. Additionally, a single point vibrometer (Polytec PDV-100) is aimed at the surface of the actuator to be used as the reference. Frequencies are measured from 1 kHz to 3 kHz in steps of 500 Hz. Complex displacement measurements (real and imaginary that can also be represented as amplitude and phase) were taken and corrected for any phase delay from the reference signal. A 3-point moving average filter was applied to reduce noise. Additionally, due to line of sight constraints, the SLDV could not measure points directly at the contact point of the actuator and finger. Therefore, a complex-valued displacement is extrapolated as the maximum amplitude and zero phase at the radius of the actuator.

2.4.2 Post Processing using Analytical Approximation

Displacement measurements were processed using MATLAB. A custom code was created using the Global Optimization Toolbox as used by Yasar *et al.* (24). Additional parameters were used as in Kearney *et al.* (18) to account for variations and incorporated into Equation 2.3 to form the objective function,

$$FRF_{obj} = X_1 e^{jX_2} \frac{I_0(jX_3(r - X_4))}{I_0(jaX_3)} + X_5, \tag{2.6}$$

where X_1 is the amplitude, X_2 is the phase offset, X_3 is the complex surface wavenumber k_{su}, X_4 is the symmetry shift, and X_5 is the zero offset. The data is fit using a least square approach. Two hundred initial guesses are used for k_{su} over a range from 10 to 2000. The optimization is run for 10 trials. Using more trials did not lead to different or better results. Once all guesses are evaluated, the least square fit (r^2) is used to determine the k_{su} with highest correlation. The resulting k_{su} is converted to a complex shear modulus using Equation 2.4 and Equation 2.5.

2.4.3 Post Processing using Viscoelastic Models

Once μ_R and μ_I are obtained using either the analytical approximation or FE-based Optimization method detailed above, best fit viscoelastic models are estimated. Using another custom MATLAB code utilizing the Global Optimization Toolbox, the storage and loss modulus simultaneously are fit to each viscoelastic model in Table I. The parameters yielding the best correlation are then selected to represent each viscoelastic model.

TABLE II: Storage and loss moduli calculated using analytical approximation

Frequency	Storage Modulus μ_R (kPa)	Loss Modulus μ_I (kPa)	R^2
1000	118.0	44.1	0.88
1500	125.9	60.7	0.78
2000	161.2	63.1	0.81
2500	155.1	46.6	0.66
3000	204.9	45.1	0.52

2.5 Results

The derived Storage and Loss Modulus are shown in Table II along with the corresponding R^2 values to show correlation. An example of the curve fit can be seen in Figure 3.

The Storage and Loss modulus were then processed to curve fit multiple viscoelastic models. Table III details the parameters derived along with R^2 values to show correlation. The model with the best fit was SLS. A plot of the fits can be seen in Figure 4.

TABLE III: Viscoelastic models based on analytical approximation

Model	1^{st} parameter	2^{nd} parameter	3_{rd} parameter	R^2
Fractional Voigt	μ_0=0.0 kPa	μ_α=21.2 kPa s^α	α=0.22	0.92
Maxwell	μ_1=92.7 kPa	η =41.2 Pa s	-	0.89
SLS	μ_0=92.7 kPa	μ_1=117.4 kPa	η=10.3 Pa s	0.96
Spring-pot	μ_α=21.2 kPa s^α	α=0.22	-	0.92
Voigt	μ_0=153 kPa	η=3.63 Pa s	-	0.78

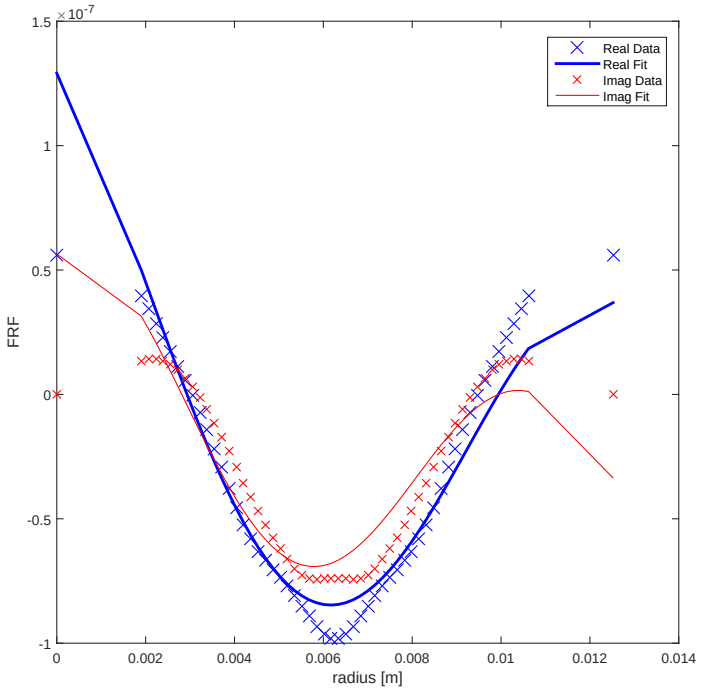

Figure 3: Analytical curve fit for experimental data at 1 kHz

2.6 Discussion

Results shown in Table II and Figure 4 illustrate that the analytical approach do not accurately model the behavior of the fingertip. The analytical model assumes a semi-infinite halfspace and actuation of an infinite cylinder going through the medium. The large errors in approximation was an area of much study to improve the experimental setup and remove any extraneous variables. Eventually the approximation was studied itself and found to be an

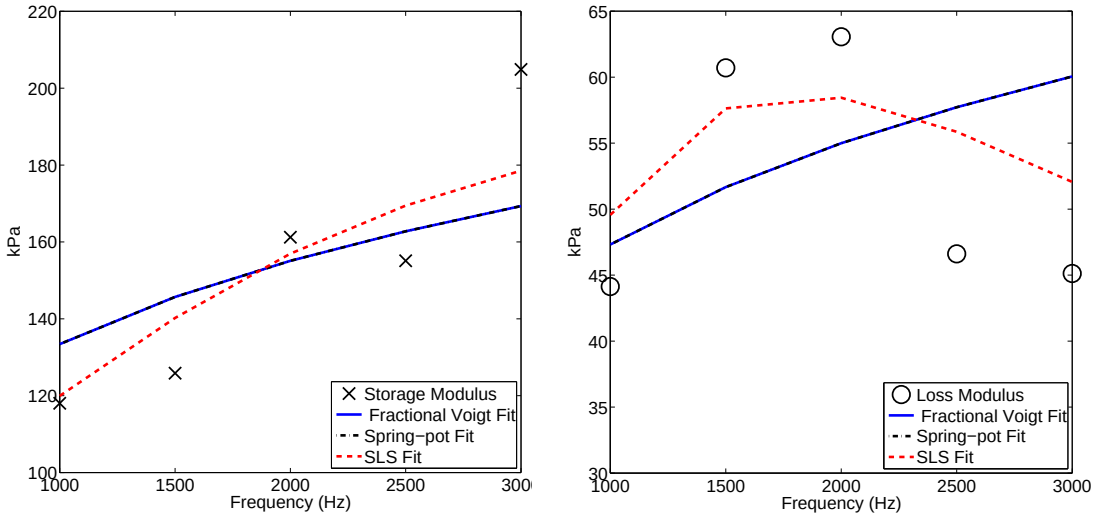

Figure 4: Viscoelastic models fit to analytical approximation of experimental data: (left) storage and, (right) loss moduli

inaccurate approximation. Therefore a new method of post processing needed to be developed.

Enter Finite element-based optimization.

CHAPTER 3

FINITE ELEMENT BASED OPTIMIZATION OF MATERIAL PROPERTIES FROM EXPERIMENTAL RESULTS

(Previously published as Khan, A., Kearney, S., Royston, T. (2018) Finite Element Based Optimization of Human Fingertip Optical Elastography, J. Medical Diagnostics 1(3), 031007)

Since the results in section 2.5 are not satisfactory, Finite element analysis (FEA) was used to further study the analytical model. FEA involves breaking down a model into smaller elements. Then physics simulations can be applied to the smaller elements with known equations and a larger approximated simulation can be derived from the summation of the elements. Using FEA is a more accurate way of solving equations where the geometry is not ideal case.

3.1 Theory: Analytical Approximation Validation

The theory covered in section 2.2 is further studied in this section. By substituting $I_n(x) = i^{-n}J_n(ix)$, where $n = 0$, into Equation 2.3 it can be rewritten in terms of Bessel function of the first kind. Since Bessel functions of the first kind and zeroth order are even functions further simplifications can be made to yield:

$$FRF = \frac{u_z(r)}{u_z(a)} = \frac{J_0(-rk_{su})}{J_0(-ak_{su})} = \frac{J_0(rk_{su})}{J_0(ak_{su})} \tag{3.1}$$

As this is equivalent to Equation 2.2, it required further study. To assess the validity of this analytical analogy FEA simulations were conducted and are presented in this dissertation.

3.2 Method

3.2.1 Evaluating analytical approximation with Finite Element optimization

To assess the validity of assumptions in the analytical approximation and FE-based optimization methods introduced in the previous sections, FE models with material properties comparable to soft biological tissue were generated and tested. Two cases are studied to see how the equations fit to semi-infinite halfspace and semi-infinite cylinder models. To reduce calculation time and memory usage, a 2D axisymmetric model was used to create a cylinder of 1 meter radius and 5 meters length to simulate the infinite halfspace. Low reflecting boundaries were used to minimize boundary effects,such as reflections and mode conversion. The material is given a springpot model to be similar to materials previously studied by our group (Yasar *et al.* 2013), where, where μ_α is 4571 Pas^α and α is 0.34. The mesh was automatically generated by COMSOL and the finest mesh was selected (30,965 triangular elements, 239 elements distributed along surface from r=0 to 4 mm, and remaining elements sized between 0.1 mm to 50 mm). The model is actuated for multiple frequencies by an 8 mm ring on the surface.

Then, to simulate a cylinder driven harmonically with a displacement at its outer radial boundary in the axial direction, the model is modified to be only 4 mm in radius and the simulation is repeated with the entire outer wall of the cylinder being actuated. Again the mesh was automatically generated by COMSOL and the finest mesh setting was selected (20,550 triangular elements, 239 elements distributed along surface from r=0 to 4 mm, and remaining elements sized between 0.1 mm to 50 mm).

3.2.2 Post Processing experimental results using FE-based optimization

A finite element model is created in COMSOL 5.3 Multiphysics in 3D space using the Solid Mechanics Module and Optimization Module in the Frequency Domain. A CAD model of the fingertip, created from segmented slices of MRI images taken using a Bruker Preclinical 7T MRI (Bruker Instruments, Billerica, MA, USA), is imported into the model. A circular ring is defined on the surface using the same dimensions as the experimental setup. The bottom of the fingertip is defined as a fixed surface. The base of the model that would connect with the rest of the finger is treated as a low reflecting boundary condition. A low reflecting boundary is a boundary condition used in COMSOL to minimize reflections from the edge, by using material data from adjacent domain in order to create a perfect impedance match for compression and shear waves. It is primarily used to reduce the computational domain to a practical size while ensuring accurate simulation results (27). Rather than simulating an actuator, the model treats the area of contact, in this case a circle on the surface, to be a prescribed displacement in the z direction, orthogonal to the surface of the fingertip. The ring is excited at a given displacement and frequency. The amplitude of displacement is selected based on measurements of the actuator during the experimental procedure. The materials are considered viscoelastic, isotropic, nearly incompressible (Poissons ratio 0.49995). The mesh is automatically generated through COMSOL's built in physics-controlled mesh (122,699 tetrahedral elements, maximum element size 0.733 mm, minimum element size 0.0314 mm). The second finest mesh setting was selected. Selecting the finest mesh possible increased computation time significantly and had a negligible impact on the results.

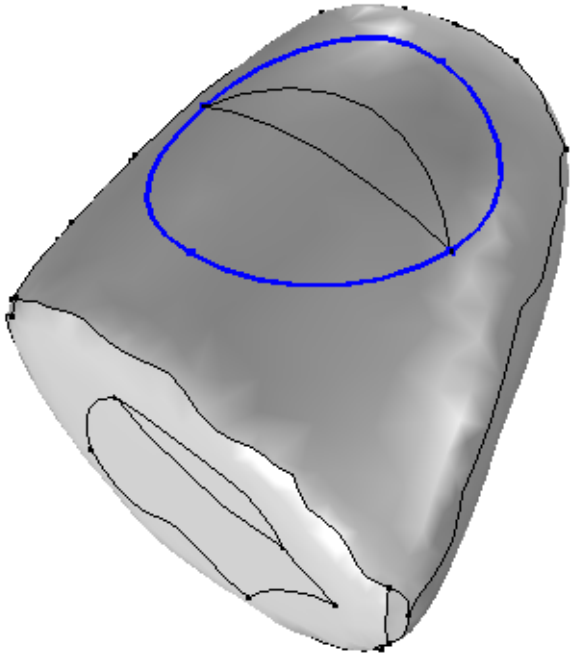

Figure 5: FE solid model of finger. Blue circle denotes actuation

Although the wave motion can be in multiple directions, the SLDV only measures motion normal to the surface of the fingertip, and measurements were taken along a radial profile within the annular region of excitation. Therefore, we only extract the displacement in the z direction from the FE simulation along this same radial profile for comparison. Displacement measurements from the SLDV are imported into COMSOL as experimental data points. A function is created from the points using interpolation to create an experimental profile to account for any gaps in measurements. The model is run through the Optimization Module where the

shear storage and loss modulus are varied. The resulting displacement is then compared to the experimental profile using,

$$\int_{-a}^{a} (v_{exp}(r) - v_{optim}(r))^2 dr * 10^{15}, \tag{3.2}$$

where v_{exp} and v_{optim} are displacement in the z direction of the experimental and FE-based optimization data, respectively. The scaling of 10^{15} at the end is to improve the sensitivity of the error function as per recommendation through COMSOL support. The optimization uses the Nelder-Mead method. The optimization tolerance is set to 0.0001 for the error function. The maximum iterations are set to 1000 although optimization completes before the maximum iteration limit is reached due to the tolerance limit.

3.3 Results

3.3.1 Evaluation of Analytical Approximation and FE Based Optimization using Synthetic Data

The resulting synthetic data of displacements seen in Figure 6 are run through the analytical curve fit procedure (Section 2.4.2) yielding results seen in Figure 7 along with the actual values of storage and loss moduli; identified viscoelastic model values can be seen in Table IV.

In place of the analytical approximation, the FE-based optimization method was applied to the same synthetic data to reconstruct material properties as well. To reduce bias, starting points for the optimization method were varied from the known material properties. Both solu-

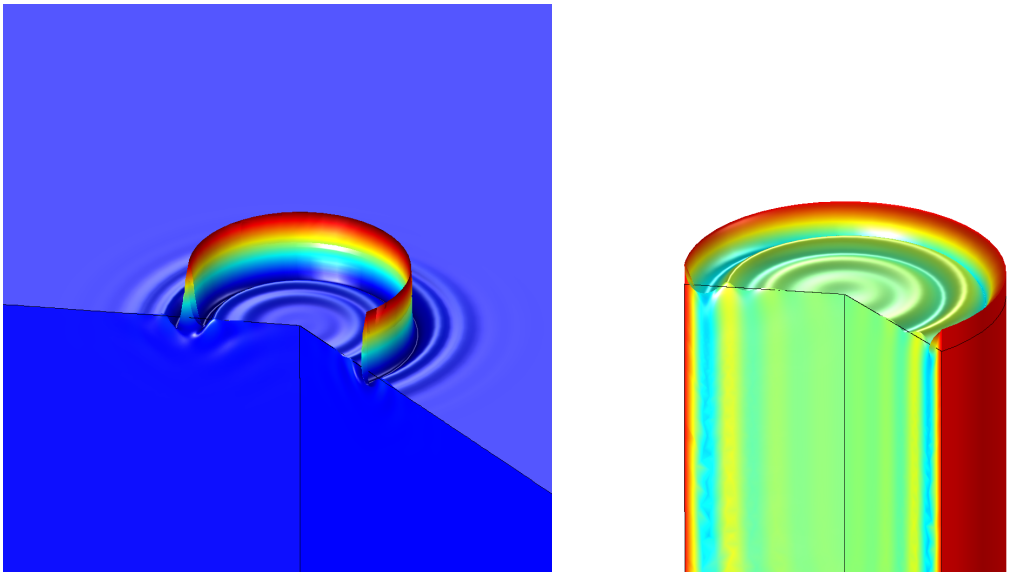

Figure 6: Wave propagation at 1 kHz for (left) ring actuator on surface and (right) cylindrical wall actuation

tions for the ring and cylindrical excitation can be found in Figure 8. Additional reconstructed values can be seen in Table IV.

3.3.2 FE-based optimization to identify viscoelastic properties based on experimental data

Experimentally measured displacements from SLDV were post-processed in COMSOL using the method detailed in Section 3.2.2. The procedure was repeated multiple times with varied initial guesses to avoid reaching a local extremum. In the rare case that a limit was reached, the limits were expanded and the initial guess was based on where the previous optimization left off. Figure 9 shows an example of the optimization output. Table V shows the derived

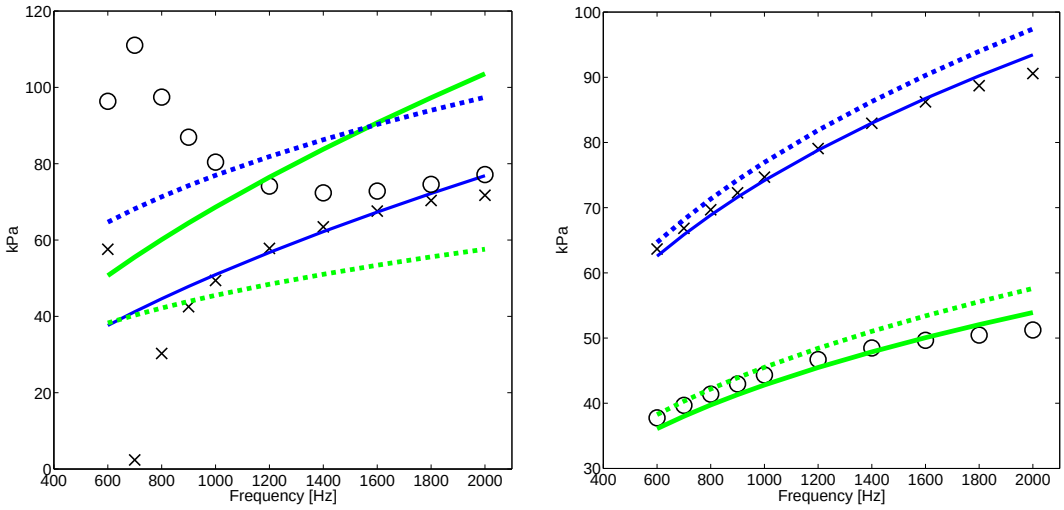

Figure 7: Identifying shear storage and loss moduli using analytical approximation: (left) ring actuator on surface; (right) cylindrical wall actuation. Key: Actual storage (blue dash) and loss (green dash) moduli; X and O best fits to storage and loss moduli, respectively, using analytical approximation. Resulting best fit rheological (springpot) model based on X and O best fits (solid lines).

Storage and Loss Modulus at each frequency. 3 kHz was rejected due to a failure to converge to an appropriate solution.

Values from Table V were used for fitting viscoelastic (rheological) models. Table VI shows the derived values for the viscoelastic models along with corresponding R^2 values to show correlation. The best fit was the SLS model while the Fractional Voigt and Spring-pot models were comparable. Their corresponding plots can be seen in Figure 10.

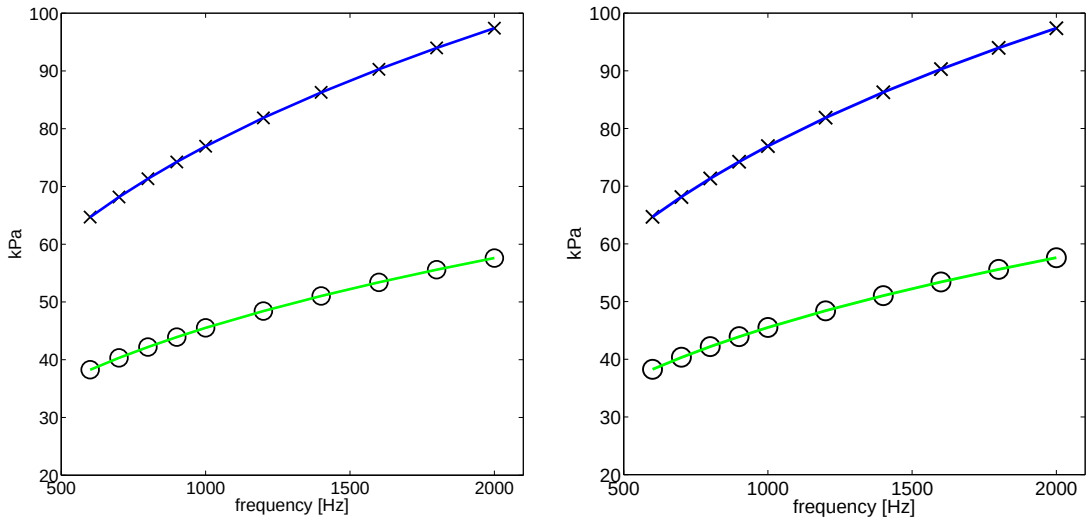

Figure 8: Identifying shear storage and loss moduli using FE-based optimization method: (left) ring actuator on surface; (right) cylindrical wall actuation. Key: Actual storage (blue dash) and loss (green dash) moduli; X and O best fits to storage and loss moduli, respectively, using FE-based optimization method. Resulting best fit rheological (springpot) model based on X and O best fits (solid line exact match and overlays the actual values)

3.3.3 Layered Materials

From Table V and Table VI, as well as Figure 10, it is clear that the simple viscoelastic models considered here that are based on an assumption of homogeneity and isotropy are a poor fit and cannot capture the frequency dependence of the apparent shear storage and loss moduli of the fingertip based on experimental measurements from 1 to 2.5 kHz. In fact, over this frequency range there is a near doubling of the shear storage modulus and an increase in shear loss modulus by more than a factor of ten. Such significant increases defy conventional models of viscoelasticity and highlight the limitation of assuming homogeneity of material properties.

TABLE IV: Viscoelastic models estimated using analytical (Sec. 2.4.2) and FE-based optimization (Sec. 3.2.2)

Model	μ_0	α	R^2
Actual	4571 Pa s^α	0.34	-
Analytically Optimized Ring	475 Pa s^α	0.59	0.015
Analytically Optimized Cylinder	4628 Pa s^α	0.33	0.99
FE Optimized Ring	4571 Pa s^α	0.34	1.00
FE Optimized Cylinder	4570 Pa s^α	0.34	1.00

TABLE V: Storage and loss moduli from an FE-based optimization

Frequency	Storage Modulus μ_R (kPa)	Loss Modulus μ_I (kPa)	Error (10^{15})
1000	92.8	3.06	0.011
1500	121	6.43	0.045
2000	131	12.3	0.201
2500	173	39.1	0.0092

To investigate this, we return to the numerical FE simulation study of Section 4.1, but modify the halfspace model by tripling the complex shear modulus for a 1 mm thick layer of the material at the surface. Using the output of the FE simulation of this layered halfspace the FE optimization routine, which assumes homogeneity, produced estimates of shear storage and loss moduli shown in Table VII. Note, the complex shear modulus of both the top 1 mm layer and the underlying layer are modeled with a Spring-pot model with α=0.34. So, from 1 to 2.5 kHz both of their storage and loss moduli should increase by a factor of $2.5^{0.34} = 1.37$. Yet, by neglecting the layering effect and assuming homogeneity, the optimization routine predicts

TABLE VI: Viscoelastic models based on FE optimization

Model	1^{st} parameter	2^{nd} parameter	3^{rd} parameter	R^2
Fractional Voigt	μ_0=96.2 kPa	μ_α=1.45 kPa s^α	α=0.35	0.89
Maxwell	μ_1=131 kPa	η =122 Pa s	-	0.85
SLS	μ_0=114 kPa	μ_1=51.7 kPa	η=3.17 Pa s	0.91
Spring-pot	μ_α=51.2 kPa s^α	α=0.10	-	0.89
Voigt	μ_0=130 kPa	η=1.59 Pa s	-	0.88

increases in shear storage and loss moduli by factors of 1.52 and 6.62. Moderate over-prediction of shear storage modulus and significant over-prediction of shear loss modulus is consistent with trends in values calculated based on the experimental fingertip measurements, which is evident in Figure 10.

TABLE VII: Storage and loss moduli from an FE-based optimization of layered materials

Frequency	Storage Modulus μ_R (kPa)	Loss Modulus μ_I (kPa)	Error (10^{15})
1000	121	4.45	0.477
1500	144	7.09	0.133
2000	163	17.5	0.060
2500	184	29.4	0.047

3.4 Discussion

The FE study in Section 3.3.1 suggests that the analytical approximation for geometrically focused surface waves caused by an annular actuator on the surface is not exact. It was also noticed that the surface wave response within the annular region was affected by the width (radial extent) of the annular actuator, which is not a factor in the analytical approximation. Nonetheless, this simple approximation, as it is, which took only a few seconds to obtain can be used to provide an initial estimate of shear viscoelasticity, which can serve as a starting point for numerical optimization using the FE-based approach. Figure 8 and Table IV show that the FE-based optimization more accurately approximates the material properties in both annular and cylindrical actuation cases. Speed and accuracy of optimization using FEA for this complex optimization problem with multiple local optima improves when the starting point is within a factor of the optimal solution.

The FE-based optimization to estimate the complex shear modulus of the fingertip, with geometry derived from ultra high field MR imaging, could be improved. By viewing an animation of the wave motion, it appears that the boundary conditions have a non-negligible influence on the propagation. Since the fingertip FE model is truncated, it would be better to extend the geometry of the fingertip to include the rest of the finger. There is a non-zero displacement near the truncation boundary, which in turn results in reflection of wave motion that would not occur in a an untruncated model. Additionally, the entire fingertip was treated as having the same homogeneous material properties. This is not accurate as the actual composition of the finger includes bone, muscle, fatty tissue, and layers of skin. Each of these would have their

own material properties. The numerical study in Section 3.3.3 highlighted how increased shear viscoelasticity near the surface is likely the reason for the significant increase in shear moduli with respect to frequency based on the FE optimization strategy that assumes homogeneity.

Although the feasibility study in this paper covers the methods of material property reconstruction, the derived values should not be considered as normal values. Multiple samples must be taken to test for repeatability. It has been seen that the air humidity as well as the moisture content of the fingertip can alter the wave propagation and therefore the material properties. Future work could involve measuring both humidity and moisture content and testing on the same volunteer on different days as well as multiple volunteers on the same day.

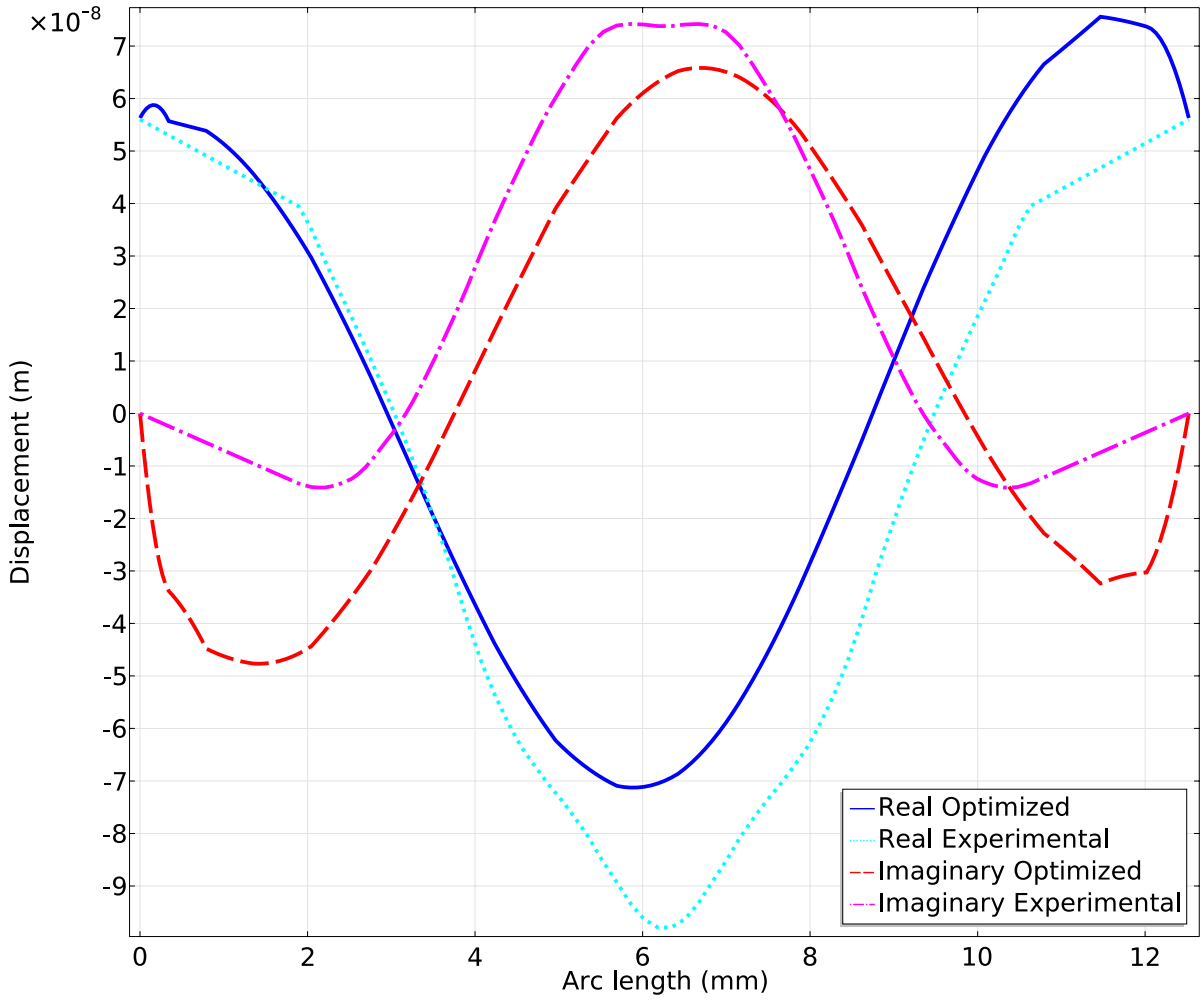

Figure 9: FEA optimization fit at 1 kHz

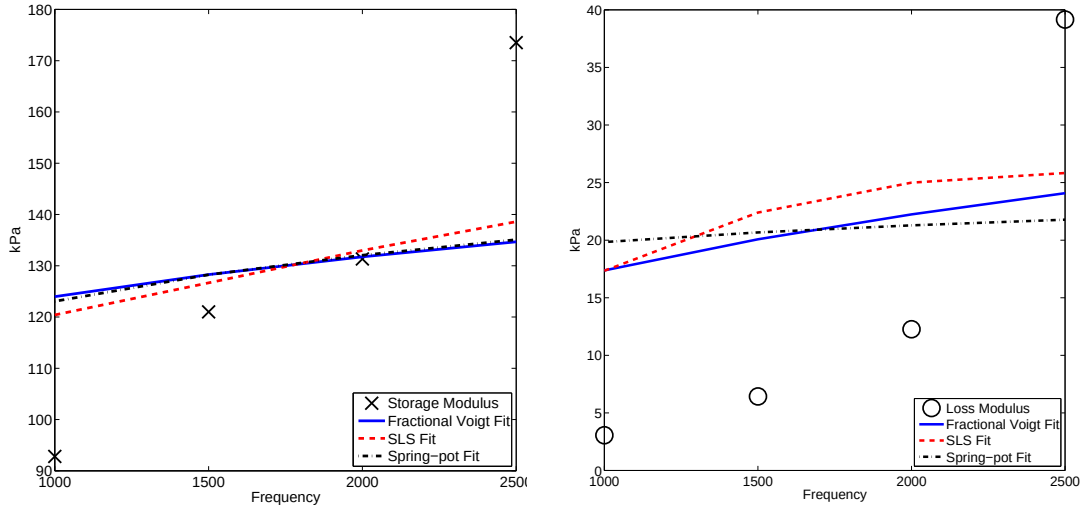

Figure 10: Best fits of different viscoelastic models to FE-based estimate of storage and loss moduli based on experimental measurements.: (left) storage and (right) loss moduli

CHAPTER 4

OPTICAL COHERENCE TOMOGRAPHY ON FINGERTIP SUBSURFACE

4.1 Background

Optical coherence tomography (OCT) takes images near the surface of an object to a small penetration depth. It is an interferometric imaging method that utilizes short coherence lengths of broadband light sources. It can penetrate up to 1-2 mm below the surface. Although ultrasound has been used in the past in elastography, OCT was first used in elastography in 1998 on a smaller scale than ultrasound (28). Although it is a light-based and optical approach like SLDV, it adds the ability to measure wave propagation below the surface. This allows us to see how structures and materials below the surface affect the wave propagation.

Optical Coherence Elastography (OCE) uses three different methods to estimate material properties: static, transient, and harmonic (15). The static method estimates elastic properties based on deformation to an applied force. Transient measures the response to an impulse force to estimate dynamic elastic properties. Finally, harmonic OCE uses low frequency vibrations, below kHz range, to measure wave propagation of shear and Rayleigh waves to estimate viscoelastic properties.

Combining OCE with the same setup used in section 2.4.1 allows us to measure wave propagation below the surface of the fingertip. Challenges with the OCT system involve taking

images at a frequency that is similar to the actuation frequency with a small offset. This is similar to using the strobe effect to visualize high frequency vibrations in a setup. The frame rate of capture severely limits the frequencies that can be measured.

4.2 Methods

The same setup described in Section 2.4.1 is used to make OCT measurements. The OCT laser is aimed at the surface of the finger. A width of 3 mm is viewed with 2-3 mm penetration below the surface. The surface is vibrated at 100 Hz and the OCT takes measurements at 52 Hz for approximately 4 seconds. The experiment is repeated at the same frequency but the OCT takes measurements at 93.3 Hz to explore the differences in imaging frame rate. Individual frames of the video are saved as images for later use in post processing.

4.3 Results

Figure 11 and Figure 12 show sample images taken from OCT. Wave propagation can be seen in each. Multiple frames were taken over the course of 1 second leading to about 1000 images. Running multiple frames as a video shows the waves traveling across the surface.

4.4 Discussion

Several challenges when working with OCT has limited the development of its research and feasibility. The frame rate severely limits the frequencies that can be measured. Increasing the frame rate of the imaging lowers the field of view and penetration depth that can be studied. Additionally, the frame rate is unable to go past 100 Hz meaning frequencies beyond that range cannot be measured or must be used in multiples of 100 Hz.

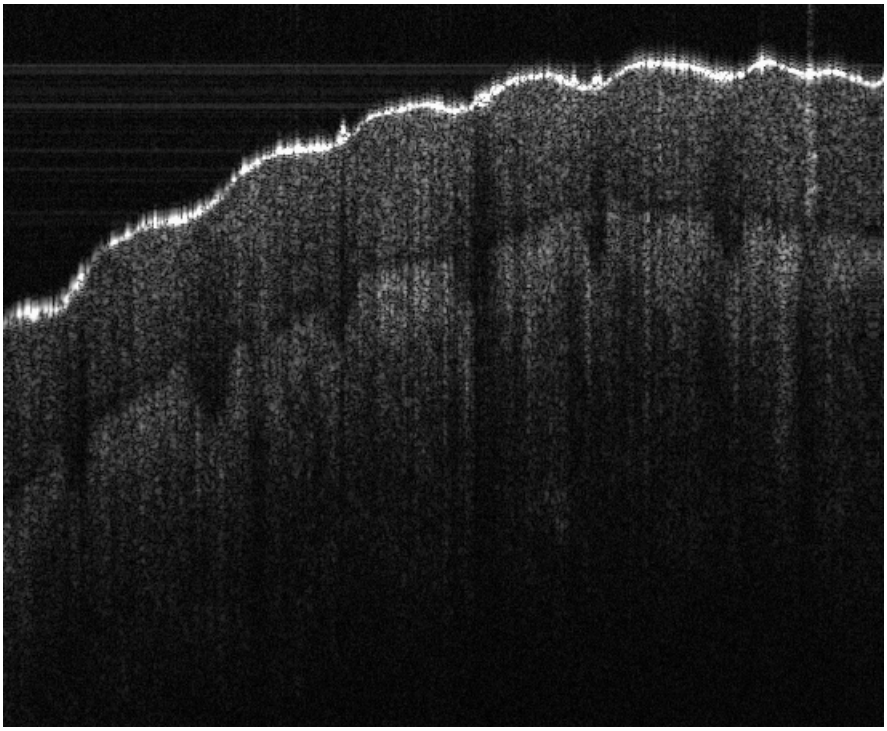

Figure 11: OCT image of finger at 100 Hz excitation and 93.3 Hz framerate

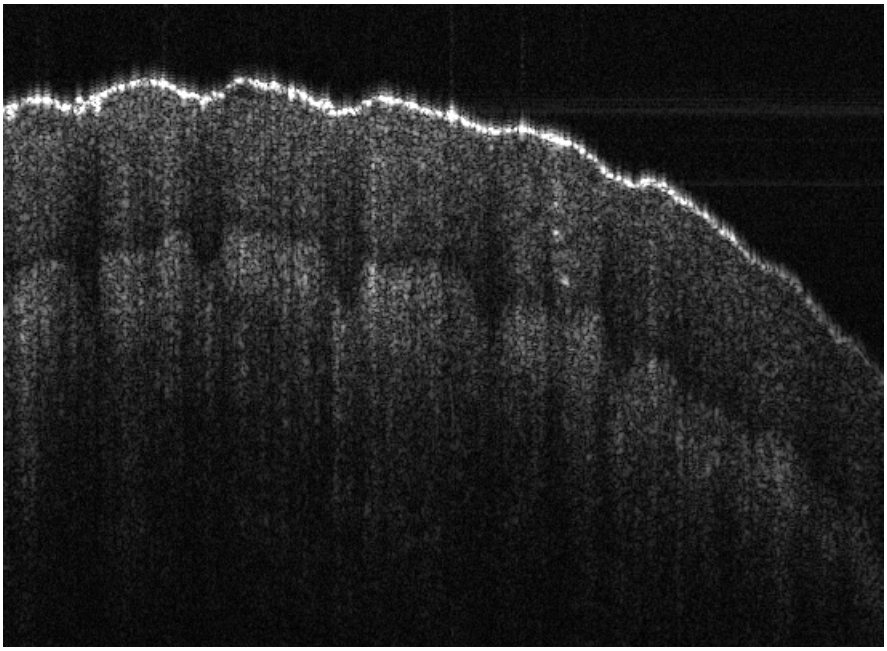

Figure 12: OCT image of finger at 100 Hz excitation and 52 Hz framerate

Beyond the frame rate, the OCT is sensitive to any motion of the finger itself. Stabilizing the finger is absolutely necessary to prevent it from shaking. Additionally, since the areas inside the finger are moving, it creates a new challenge of tracking the motion of each specific point inside the finger over a period of time. SLDV and MRE are able to track the points making it easier to follow its motion over time. Therefore, there is much work needed to be done in the OCT field which extends beyond the scope of a single Ph.D degree.

CHAPTER 5

MAGNETIC RESONANCE IMAGING ON FINGERTIP AND SURFACE COIL DESIGN

5.1 Background

Magnetic resonance elastography (MRE) is an MRI technique that can used to estimate material properties of subdermal tissue. Mechanical waves are generated on the surface of the body nearest to the tissue being studied. The resulting wave propagation is encoded in the phase image through the use of motion encoding gradients (MEG). The wave propagation can be inverted to estimate material properties such as shear stiffness. It has been shown that tissue stiffness is related to tissue health.

One of the biggest challenges when working with MRE is the mechanical set up in a high magnetic field. All parts need to be non-magnetic. Additionally, at high fields a small bore diameter for the magnet generally constrains the setup further. Finally, due to the use of RF coils, the actuators generally cannot be placed in the optimal position to excite the area being studied. Therefore, the design of RF coils that incorporated MRE actuators was studied to image the fingertip.

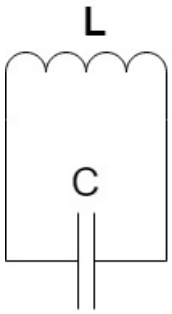

Figure 13: Basic RF coil design

5.2 Theory

5.2.1 Theory: RF Coils

The most basic RF coil consists of an inductor and a capacitor (29) as seen in Figure 13. Its resonant frequency is determined Equation 5.1:

$$\omega = \frac{1}{\sqrt{LC}}, \tag{5.1}$$

where ω is resonant frequency in rad/s, L is inductance, and C is capacitance. The resonant frequency should be closely matched to the frequency, f (Hz), of the magnet determined by Equation 5.2:

$$f = \frac{\omega}{2\pi} = \gamma B_0, \tag{5.2}$$

where γ is the gyromagnetic ratio specific to the nucleus of the atom being studied and B_0 is the magnetic field strength of the magnet. The gyromagnetic ratio for hydrogen, the nucleus being imaged, is 42.58 MHz/T and the B_0 of the magnet is 9.4T making the frequency 400 MHz.

Since each sample being imaged has differences in impedances, a tuning matching circuit is added to optimize energy transfer between the sample and the coil as seen in Figure 14. C_T and C_M represent variable capacitors used to tune and match the coil respectively.

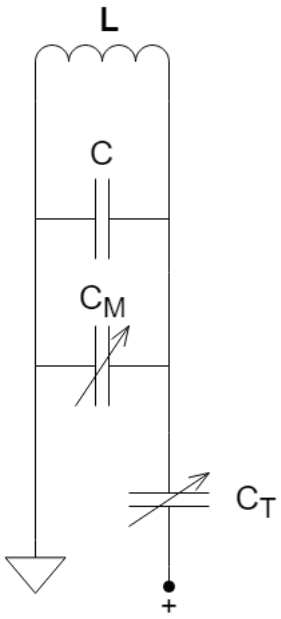

Figure 14: RF coil design with tuning and matching circuit

5.2.2 Theory: MRE

MRE measures phase accumulation, ϕ, of waves using motion encoding gradients (MEG). It is given by the time integral of the dot product of the motion r and MEG strength, G:

$$\phi = \gamma \int_0^\tau G(t) \cdot r(t) dt, \tag{5.3}$$

where τ is the time duration of the gradients after excitation and r(t) represents of the nuclear spins as a function of time (30). To measure how the wave propagates over a period of time, a phase offset can be added to either G(t) or r(t). Generally this is done at value equal to the period of the frequency divided by an interval of 8 to get 8 time steps. The direction of motion encoding is determined by the MEG used. SampLe Interval Modulation MRE (SLIM-MRE) can be used to encode motion encoding in all spatial directions simultaneously to save time (31).

5.3 Methods

5.3.1 Methods: Designing the RF Coil

The first coil designed was a birdcage coil using 6 rungs in high pass filter configuration. A coil pattern was etched on copper sheet using Press-N-Peel Blue PCB Film (Techniks Inc. Ringoes, NJ, USA) and ferric chloride acid. The sheet was affixed to a fiberglass tube using Stycast 1266 epoxy (Henkel Loctite Rancho Dominguez, CA, USA). Capacitors (Johanson Technology, Camarillo, CA) were placed along the end rungs and a tuning matching circuit was created using two tunable capacitors. Pick up loops were used to measure the resonance

of each window using a network analyzer. The coil was adjusted and modified to bring the coil to as close as possible to the correct resonant frequency (400 MHz). Holes were drilled through the coil to allow the actuators to pass through inside without damaging the RF components. A piezoceramic actuator is affixed underneath the coil allowing it to directly apply actuation to the fingertip in a straight line.

When complete, a water-based sample was placed inside the coil and placed inside the MRI. Due to the complexity of the birdcage coil, the resonant frequencies of each individual window of the birdcage coil varied enough to cause a drastic drop in SNR. Therefore, we were unable to obtain any images using this coil.

To reduce the complexity of the coil, a surface foil was designed and built. An oval shape is cut out of copper tape using a Cricut Maker (Provo Craft, Spanish Fork, UT) and placed on a bed designed in SOLIDWORKS (Dassault Systèmes, Concord MA) and 3D printed out of polylactic acid (PLA) using a Makerbot Fifth Generation printer (Stratsys, New York City, NY). Two capacitors of equivalent value are placed in the circuit and the resonant frequency is measured using pick up loops and a network analyzer. Once the coil was built to resonate at 400 MHz, one capacitor was replaced by one of lower value and placed in parallel with a variable capacitor and connected to a tuning matching circuit. The coil was placed on a bed and a piezoceramic actuator was affixed underneath as seen in Figure 15.

5.3.2 Methods: Finger MRE

The coil was placed in the center of a Agilent 9.4 T small animal scanner (Agilent Technologies, Santa Clara, CA). The largest set of gradients (210 mm bore) were used as the arm

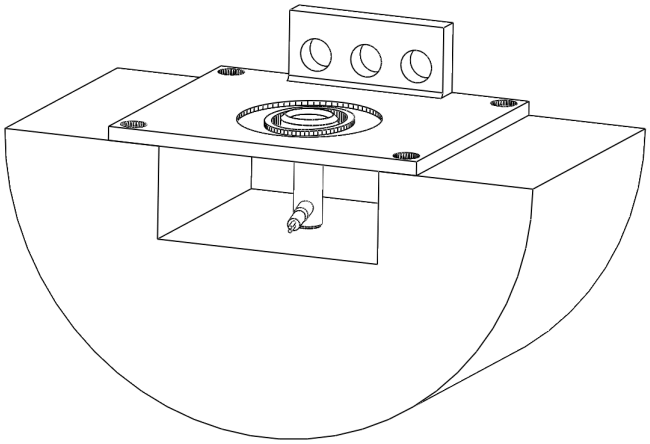

Figure 15: 3D model of surface coil and MRE actuator setup

of the volunteer needed to reach the center of the magnet, approximately one meter from the end. The volunteer, aka the author, placed their finger on the coil by reaching through the bore. The arm inside the bore was supported to reduce shaking.

Initial scans used gradient echo sequences to create 10 localization images along the length of the fingertip using 1 mm slice thickness. To reduce the time of the experiments, only one slice was used for MRE. Based on localization images the slice that contains the center of the actuator was used selected for MRE. Frequencies for 1000, 1500, and 2000 Hz were selected for study to match experiments done in SLDV. Running gradients at 2000 Hz led to overheating gradients and was eventually aborted while running 1000 Hz experiments required a minimum echo time (TE) to be much higher leading to low quality imaging. Eventually only 1500 Hz was studied. For the MRE scans, SLIM sequences are used to image motion in all directions

simultaneously and reduce scan time. Field of view (FOV) was set to 1.3 cm by 2.6 cm and with 96 by 192 resolution resulting in square pixels. Slice thickness was 2 mm. Repetition time (TR) was set to 31 msec and TE was 9 msec. 5 and 8 MEGs were used in the scans. 8 time steps are taken with 180° phase offsets for static noise subtraction. Imaging time was approximately 1 minute.

Post processing of results was done using MREDeviant (UIC Acoustics and Vibrations Laboratory, Chicago, IL). A mask was applied to remove the background and bone. All directions of motion are processed and a video is made of the wave propagation.

5.4 Results

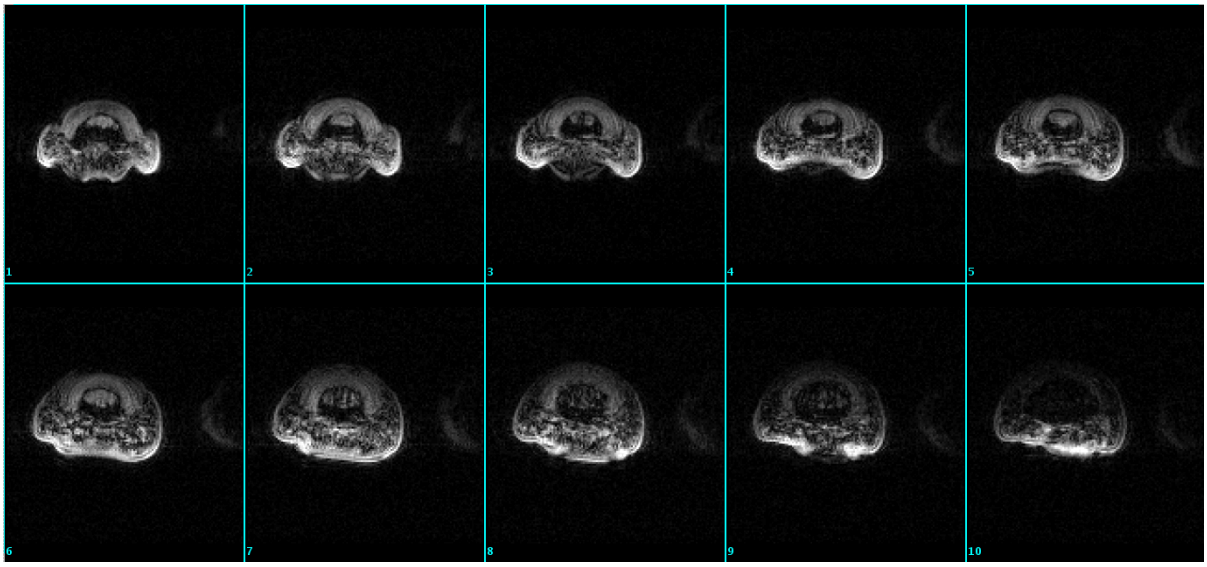

Figure 16: MRI axial images of fingertip along its length

Figure 16 shows the localization images taken using gradient echo sequences. The superior portion of the image shows the fingernail and the inferior is where the actuator comes in contact with the fingertip as well as the surface coil. Images start from the tip of the finger and work through its length for each slice. The 8th slice is chosen for MRE. Figure 17 shows wave propagation in the y direction. The red arrows denote where the actuator comes in contact with the fingertip, as well as its direction of travel. The bone and background have been masked out of the image.

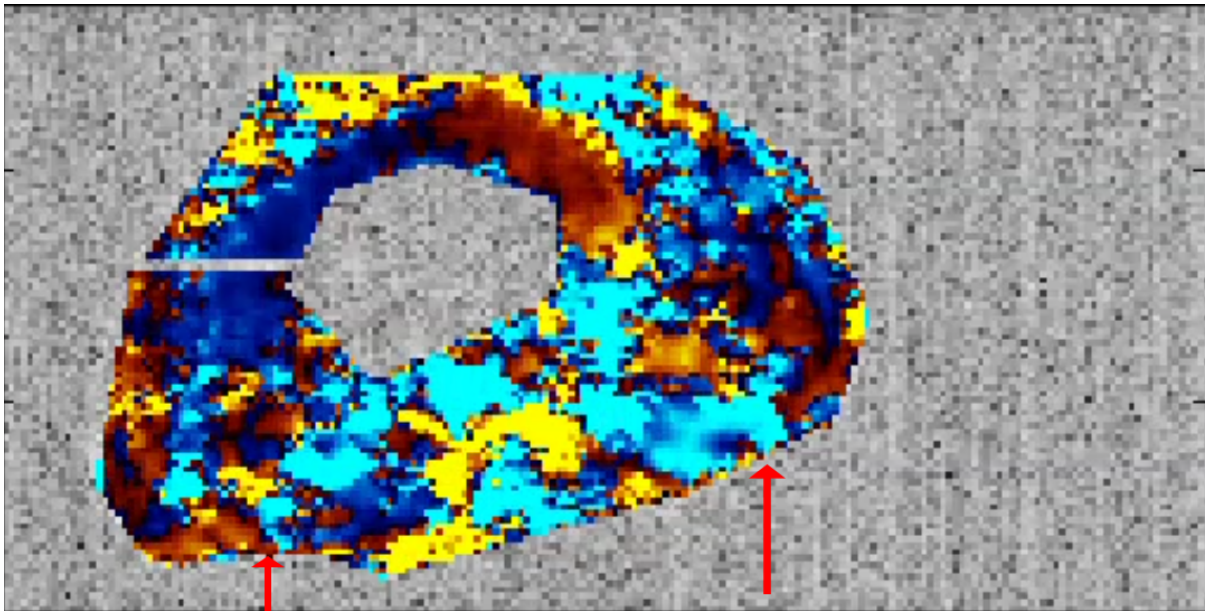

Figure 17: MRE image of fingertip. Red arrows denotes where actuator contacts the fingertip.

5.5 Discussion

The RF coil has worked well for the purposes of the experiment. As seen in Figure 16, the anatomy of the finger can be clearly made out including the interaction of the fingernail, the soft tissue, hard tissue, the fat content on the pad of the fingertip, and the actuator contact points. Artifacts can be seen on the sides as a result of using a much larger gradient than the RF coil.

MRE itself has shown that wave propagation on the fingertip is much more complex than previously anticipated. The fat content creates multiple interferences such as refraction and reflections. The wavelengths around the hard tissue near the fingernail and bone are much more consistent showing that the MRE is working properly. This adds to the claim in section 3.3.3 that the fingertip needs multiple layers and material properties to properly model its behavior.

The RF coil and actuator setup has proven its usefulness in simultaneously imaging and vibrating an area of interest. It can be further applied to other areas of the body. Additionally, it can be improved to a volume coil in order to image larger areas with high signal to noise ratio (SNR). Using smaller and more powerful gradients can improve the signal quality as well as increase the range of frequencies that can be studied. A limitation of the 9.4 T magnet is its long bore length. By using a shorter bore magnet, more parts of the body can be imaged as they can reach the center more easily.

CHAPTER 6

CONCLUSION

This dissertation has shown the implementation of multi-modal elastography on the human fingertip. SLDV, OCT, and MRI were used to measure wave propagation across the fingertip using GF waves. Additionally, FE-based optimization was used in the case of SLDV to estimate material properties of the human fingertip. To use MRI, an RF coil was designed that incorporated MRI and MRE components in one setup.

In the SLDV study, multiple frequencies were measured in order to obtain viscoelastic material properties. The wave propagation was curve fit to an analytical approximation to estimate stiffness values at a given frequency. The resulting stiffness values were then fit to multiple viscoelastic models to find the best fit. Although SLS was identified as the best fit, looking at the results showed that the analytical approximation was not an accurate model to use.

FE-based optimization was used to process the SLDV results. Creating a 3D model of the fingertip and replicating the experimental setup in COMSOL allowed the generation of wave propagation based on a set of material properties. The material properties were then optimized to best fit the simulated wave propagation to the experimental results. Material properties obtained through this method showed a vast improvement in viscoelastic models. Further studies showed that treating the finger as multiple layers of materials would improve the material properties obtained.

OCT measurements were taken using the same setup as SLDV with the exception of the OCT measurement head. Images were taken at a framerate of 52 and 93 fps. Fingertip was excited at 100 Hz. It is clear that wave propagation can be measured in the fingertip and that the layers of skin can be distinguished in the images. OCT proves worth in further study.

To incorporate MRE using the fingertip, a custom RF coil was designed that incorporates the actuator. After several iterations of coil design a surface coil was perfected and used to measure fingertip wave propagation. Limitations of the gradient size prevented a wideband of frequencies to be used but wave propagation could be seen. It is fairly evident that the fat tissue below the skin plays a large role in wave propagation as it creates refractions, diffractions, and reflections. This adds proof to the theory that the FE-based optimization needs to be treated as a multi-material model instead of homogenous.

APPENDICES

Appendix A

IRB APPROVAL

Approval Notice
Continuing Review

February 15, 2018

Thomas Royston, PhD
Bioengineering
SEO 212
M/C 063
Chicago, IL 60612
Phone: (312) 413-7558 / Fax: (312) 996-5921

RE: Protocol # 2013-0441
"HCC: Medium: Collaborative Research: Force Feedback for Fingertips"

Dear Dr. Royston:

Your Continuing Review was reviewed and approved by the Expedited review process on February 15, 2018. You may now continue your research.

Please note the following information about your approved research protocol:

Protocol Approval Period:	February 19, 2018 - February 19, 2019
Approved Subject Enrollment #:	24
Performance Sites:	Northwestern University, UIC
Sponsor:	National Science Foundation
PAF#:	00024353
Grant/Contract No:	IIS-1302517
Grant/Contract Title:	HCC: Medium: Collaborative Research: Force Feedback for Fingertips

Research Protocol(s):

a) Force Feedback for Fingertips: Protocol, Protocol Version #3, 1/14/13

Recruitment Material(s):

a) N/A- Study closed to enrollment

Informed Consent(s):

a) N/A- Study closed to enrollment

Your research meets the criteria for expedited review as defined in 45 CFR 46.110(b)(1) under the following specific category:

(4) Collection of data through noninvasive procedures (not involving general anesthesia or sedation) routinely employed in clinical practice, excluding procedures involving X-rays or

Appendix A (Continued)

microwaves. Where medical devices are employed, they must be cleared/approved for marketing. (Studies intended to evaluate the safety and effectiveness of the medical device are not generally eligible for expedited review, including studies of cleared medical devices for new indications.)

Please note the Review History of this submission:

Receipt Date	Submission Type	Review Process	Review Date	Review Action
02/14/2018	Continuing Review	Expedited	02/15/2018	Approved

Please remember to:

→ Use your **research protocol number** (2013-0441) on any documents or correspondence with the IRB concerning your research protocol.

→ Review and comply with all requirements on the guidance,
"UIC Investigator Responsibilities, Protection of Human Research Subjects"
(http://tigger.uic.edu/depts/ovcr/research/protocolreview/irb/policies/0924.pdf)

Please note that the UIC IRB has the prerogative and authority to ask further questions, seek additional information, require further modifications, or monitor the conduct of your research and the consent process.

Please be aware that if the scope of work in the grant/project changes, the protocol must be amended and approved by the UIC IRB before the initiation of the change.

We wish you the best as you conduct your research. If you have any questions or need further help, please contact OPRS at (312) 996-1711 or me at (312) 413-1835. Please send any correspondence about this protocol to OPRS via OPRS Live.

Sincerely,

Kerry A. Day, BA
IRB Coordinator, IRB # 3
Office for the Protection of Research Subjects

cc: OVCR Administration, M/C 672

UNIVERSITY OF ILLINOIS AT CHICAGO
Office for the Protection of Research Subjects
201 AOB (MC 672)
1737 West Polk Street
Chicago, Illinois 60612
Phone (312) 996-1711

Appendix B

ASME JOURNAL PERMISSION

Rights and Permissions

ASME Journals Digital Submission Tool Guidelines and Information

Rights and Permissions

Assignment of Copyright

ASME requests that authors/copyright owners assign copyright to ASME in order for a journal paper to be published by ASME. Authors exempt from this request are direct employees of the U.S. Government, whereby papers are not subject to copyright protection in the U.S., or non-U.S. government employees, whose governments hold the copyright to the paper.

For more information on copyright, please view the Copyright Transfer information page.

Retained Rights of Authors

Authors retain all proprietary rights in any idea, process, procedure, or articles of manufacture described in the Paper, including the right to seek patent protection for them. Authors may perform, lecture, teach, conduct related research, display all or part of the Paper, and create derivative works in print or electronic format. Authors may reproduce and distribute the Paper for non-commercial purposes only. Non-commercial applies only to the sale of the paper per se. For all copies of the Paper made by Authors, Authors must acknowledge ASME as original publisher and include the names of all author(s), the publication title, and an appropriate copyright notice that identifies ASME as the copyright holder.

Permissions

Once your paper has been published by ASME, you may wish to submit it for inclusion in a non-ASME publication or to incorporate some or all of its elements in another work. Since ASME is the legal holder of copyright for its papers, it will be necessary for you to secure the permission of the copyright holder to have its material published in another source.

In this case, for permission to have your paper - in whole or in part, as is or adapted - published elsewhere, please submit your request here.

Questions

The ASME Publishing staff is available to discuss current ASME policy on permissions and rights. Please feel free to contact us

CITED LITERATURE

1. Khan, A., Kearney, S., and Royston, T.: Finite element based optimization of human fingertip optical elastography. Journal of Engineering and Science in Medical Diagnostics and Therapy, 1(3):031007, 2018.

2. Dobrev, H.: In vivo study of skin mechanical properties in raynaud's phenomenon. Skin Research & Technology, 13(1):91–94, 2007.

3. Zhang, X., Osborn, T., Pittelkow, M., Qiang, B., and Kinnick, R.and Greenleaf, J.: Quantitative assessment of scleroderma by surface wave technique. Medical Engineering & Physics, 33(1):31–37, 2011.

4. Sedky, M., Fawzy, S., Baki, N., Eishi, N., and Bohy, A.: Systemic sclerosis: an ultrasongraphic study of skin and subcutaneous tissue in relation to clinical findings. Skin Research & Technology, 19(1):78–84, 2013.

5. Christensen, M., Hargens, C., Nach, S., and Gans, E.: Viscoelastic properties of intact human skin: instrumentation, hydration effects, and the contribution of the stratum corneum. Journal of Investigative Dermatology, 69(3):282–286, 1977.

6. Potts, R., Chrisman, D., and Buras, E.: The dynamic mechanical properties of human skin in vivo. Journal of Biomechanics, 16(6):365–372, 1983.

7. Ridge, M. and Wright, V.: A bio-engineering study of the mechanical properties of human skin in relation to its structure. British Journal of Dermatology, 77(12):639–649, 1965.

8. Agache, P., Monneur, C., Leveque, J., and Rigal, J.: Mechanical properties and young's modulus of human skin in vivo. Archives of Dermatological Research, 269(3):221–232, 1980.

9. Diridollou, S., Vabre, V., Berson, M., Vaillant, L., Black, D., Lagarde, J., Gregoire, J., Gall, Y., and Patat, F.: Skin ageing: changes of physical properties of human skin in vivo. International Journal of Cosmetic Science, 23(6):353–362, 2001.

10. Khatyr, F., Imberdis, C., Vescovo, P., Varchon, D., and Lagarde, J.: Model of viscoelastic behaviour of skin in vivo and study of anisotropy. Skin Research & Technology, 10(2):96–103, 2004.

11. Pereira, J., Mansour, J., and Davis, B.: Dynamic measurement of viscoelastic properties of skin. Journal of Biomechanics, 24(2):157–162, 1991.

12. Dobke, M., DiBernardo, B., Thompson, R., and Usal, H.: Assessment of biomechanical skin properties: is cellulitic skin different? Aesthetic Surgery Journal, 22(3):260–266, 2002.

13. Elleuch, K., elleuch, R., and Zahouani, H.: Comparison of elastic and tactile behavior of human skin and elastomeric materials through tribological tests. Polymer Engineering & Science, 46(12):1715–1720, 2006.

14. Luebberding, S., Krueger, N., and Kerscher, M.: Mechanical properties of human skin in vivo: a comparative evaluation in 300 men and women. Skin Research & Technology, 20(2):127–135, 2014.

15. Larin, K. and Sampson, D.: Optical coherence elastography - oct at work in tissue biomechanics. Biomedical Optics Express, 8(2):1172–1202, 2017.

16. Liang, X. and Boppart, S.: Biomechanical properties of in vivo human skin from dynamic optical coherence elastography. IEEE transactions on Biomedical Engineering, 57(4):953–959, 2010.

17. Mohan, K. and Oldenburg, A.: Elastography of soft materials and tissues by holographic imaging of surface acoustic waves. Optics Express, 20(17):18887–18897, 2012.

18. Kearney, S., Khan, A., Dai, Z., and Royston, T.: Dynamic viscoelastic models of human skin using optical elastography. Physics in Medicine & Biology, 60(17):6975–6990, 2015.

19. Sinkus, R., Tanter, M., Catheline, S., Lorenzen, J., Kuhl, C., Sondermann, E., and Fink, M.: Imaging anisotropic and viscous properties of breast tissue by magnetic resonance elastography. Magnetic Resonance in Medicine, 53(2):372–387, 2005.

20. Zhang, Y., Oberai, A., Barbone, P., and Harari, I.: Solution of time-harmonic viscoelastic inverse problem with interior data in two dimensions. International Journal for Numerical Methods in Engineering, 92(13):1100–1116, 2012.

21. Zhang, X.: A noninvasive surface wave technique for measuring finger's skin stiffness. Journal of Biomechanics, 68:115–119, 2018.

22. eds. T. Watanabe and S. Fukui A method for controlling tactile sensation of surface roughness using ultrasonic vibration.

23. Wiertlewski, M., Friesen, R., and Colgate, J.: Partial squeeze film levitation modulates fingertip friction. Proceedings of the National Academy of Sciences of the United States of America, 113(33):9210–9215, 2016.

24. Yasar, T., Royston, T., and Magin, R.: Wideband mr elastography for viscoelasticity model identification. Magnetic Resonance in Medicine, 70(2):479–489, 2013.

25. Royston, T., Mansy, H., and Sandler, R.: Excitation and propagation of surface waves on a viscoelastic half-space with application to medical diagnosis. The Journal of the Acoustical Society of America, 106(6):3678–86, 1999.

26. Graff, K.: Wave Motion in Elastic Solids.

27. Cohen, M., Jennings, P., Nach, S., and Gans, E.: Silent boundary methods for transient analysis. Computational Methods for Transient Analysis, 1:Chapter 7, 1983.

28. Schmitt, J.: Oct elastography: imaging microscopic deformation and strain of tissue. Optics Express, 3(6):199–211, 1998.

29. Mispelter, J., Lupu, M., and Briguet, A.: NMR Probeheads for Biophysical and Biomedical Experiments.

30. Muthupillai, R., Lomas, D. J., Rossman, P. J., Greenleaf, J. F., Manduca, A., and Ehman, R. L.: Magnetic resonance elastography by direct visualization of propagating acoustic strain waves. Science (80-.), 269(5232):1854–1857, 1995.

31. Klatt, D., Yasar, T. K., Royston, T. J., and Magin, R. L.: Sample interval modulation for the simultaneous acquisition of displacement vector data in magnetic resonance elastography: theory and application. Phys. Med. Biol., 58(24):8663, 2013.

VITA

Education

PhD in Mechanical Engineering	University of Illinois at Chicago	August 2018 Chicago, IL
BS in Mechanical Engineering	University of Illinois at Chicago	May 2010 Chicago, IL

Research and Teaching Experience

Research Assistant	Department of Mechanical Engineering at University of Illinois at Chicago	August 2010—Present Chicago, IL
Teaching Assistant	Department of Mechanical Engineering at University of Illinois at Chicago	January 2014 – Present Chicago, IL
Adjunct Faculty	College of Engineering at Oakton Community College	June 2018 – Present Des Plaines, IL
Mechanical Engineering Lead Instructor	Women in Engineering Summer Program	June 2016 – August 2016 Chicago, IL

Student Affairs Experience

Senior Student Staff	Department of Campus Housing at University of Illinois at Chicago	August 2009—Present Chicago, IL

Publications and Conferences

- Finite Element-Based Optimization of Human Fingertip Optical Elastography
  - Journal of Engineering and Science in Medical Diagnostics and Therapy, August 2018
- Fingertip Optical Elastography
  - Acoustical Society of America Conference, May 2018
- Scattering and Diffraction of Elastodynamic Waves in a Concentric Cylinder Phantom for MR Elastography
  - IEEE Transactions on Biomedical Engineering
- Dynamic Viscoelastic Models of Human Skin Using Optical Elastography
  - Journal of Physics in Medicine and Biology, September 2015
- Elastography Methods Applicable to the Eye
  - SPIE Conference, February 2014
- Localized Elastography Map of Human Cornea Through Surface Vibrations
  - IMECE Conference, November 2013
- Measuring and Modeling Elastography of Human Cornea using Scanning Laser Doppler Vibrometry
  - Summer Bioengineering Conference, June 2013

Awards

- Chancellor's Student Service and Leadership Award
  - April 2016
  - April 2015
- Student Employee All-Star Winner
  - April 2016
- Best Paper: Localized Elastography Map of Human Cornea
  - IMECE Conference, November 2013